Capillary Pressure Saturation Relations for PEM Fuel Cell Gas Diffusion Layers

Journal of The Electrochemical Society, **155** (11) B1225-B1231 (2008)
0013-4651/2008/155(11)/B1225/7/$23.00 © The Electrochemical Society

Capillary Pressure Saturation Relations for PEM Fuel Cell Gas Diffusion Layers

Kevin G. Gallagher,[a,*,z] Robert M. Darling,[b,] Timothy W. Patterson,[b] and Michael L. Perry[b,**]**

[a]*School of Chemical and Biomolecular Engineering, Georgia Institute of Technology, Atlanta, Georgia 30332, USA*
[b]*UTC Power, South Windsor, Connecticut 06074, USA*

Capillary pressure saturation relations (CPSRs) are presented for Toray TGP-H-060 and Mitsubishi rayon carbon fiber paper which can both be used as gas diffusion layers (GDLs) in proton-exchange membrane fuel cells (PEMFCs). The saturation is measured using water over a range of capillary pressures. Boundary and scanning curves for imbibition and drainage are measured to further understand the hysteresis observed during PEMFC operation. The primary source of hysteresis in CPSRs is attributed to the difference in advancing and receding contact angles. The measured hysteresis is predicted to have a significant effect on mass transport in the GDL and thus performance in PEMFCs.
 [DOI: 10.1149/1.2979145]

Manuscript submitted June 13, 2008; revised manuscript received August 11, 2008. Published September 25, 2008.

Water management is a critical aspect of the operation of proton-exchange membrane fuel cells (PEMFCs).[1] Typical membranes utilized in PEMFCs require high relative humidity to maintain adequate conductivity. However, this requirement must be balanced by the need to remove product water generated at the catalyst layer. In the membrane phase, water is dragged with each proton that is conducted due to electro-osmosis and diffusion occurs due to the ensuing activity gradient. In the porous diffusion media or gas diffusion layer (GDL), reactant gases must be transported to the catalyst layer while water vapor and/or liquid transport is also occurring. The GDL is typically composed of carbon fiber paper or cloth which meets the mechanical, thermal, electronic, and mass-transport requirements of PEMFCs.[2] A significant body of work exists in the published literature on the measurement and modeling of these transport properties in PEMFCs.[3,4]

Transport in the GDL may be treated with the physics of two-phase immiscible flow used in the field of porous media.[3,4] The pores are often idealized as cylindrical capillaries, allowing analysis with the Young–Laplace equation (Y-LE)[5]

$$P_c = P_{nw} - P_w = \frac{2\gamma \cos(\theta)}{r} \quad [1]$$

The capillary pressure, P_c, is related to the surface tension of the liquid, γ, the resulting contact angle, θ, and the capillary radius, r. The capillary pressure is the difference in pressure between the nonwetting fluid, P_{nw}, and the wetting fluid, P_w. For the purposes of this work, we take the gas phase to be the nonwetting phase and the liquid phase to be the wetting phase.

Although the Y-LE is indispensable for ascribing physical insight into the behavior in porous media, a more meaningful discussion of PEMFC GDLs involves a discussion of the relationship between the capillary pressure and saturation level (CPSR). The saturation or fill level of the GDL is required to determine the permeability of the liquid phase and the open porosity for gaseous diffusion. At high saturations, the PEMFC is said to be flooding and the limiting current is significantly reduced from restricted oxygen flux.[6,7] The saturation is defined as the fraction of pore volume filled with liquid

$$S_w = \frac{V_w}{V_p} \quad [2]$$

where V_w is the volume of water in the GDL and V_p is the volume of the pores.

The saturation and capillary pressure are typically related with a modified form of the Y-LE, an entirely empirical function or semi-empirical function such as the Leverett function. Using the method of standard porosimetry (MSP),[8] Kumbur et al. correlate the octane drainage curves of PEMFC GDLs with a modified form of the Leverett function for changes in wettability, compression, and temperature.[9-11] In an effort to specifically account for the geometry of the porous media, pore network models of GDLs have also been used to create CPSRs.[12-14] Another approach is the statistical calculation of a bundle of capillaries.[7] This calculation allows the direct manipulation of pore radii or interfacial tension distributions which may result in an improved understanding of the limiting factors in PEMFC performance.

Although many models exist for PEMFCs, the modeling of hysteresis in CPSR has not been included in published fuel cell models. The lack of experimental measurements of GDL CPSRs is most likely the cause of this omission. Using MSP, drainage curves with octane and imbibition curves with water have been presented.[9-11,15] Fairweather et al. have shown the difference in the boundary imbibition and drainage curves for water in PEMFC GDLs.[16] Other researchers have found no hysteresis evident in the CPSR.[17] Further work is needed to understand the cause, size, and effect of hysteresis in GDLs.

Experimental

Materials.— A number of different carbon papers are commercially available and used in PEMFC design. We have chosen to present two samples with different properties as representative of some of the possible GDLs currently used. TGP-H-060 was purchased from Toray Industries, Inc., and is referred to simply as Toray. Carbon fiber paper was also purchased from Mitsubishi Rayon Corporation and is referred to as MRC. The measured uncompressed thicknesses of Toray and MRC are 0.19 and 0.12 mm, respectively. GDLs were evaluated both as-received (AR) and after a wet-treating (WT) process. The WT-GDLs are rendered hydrophilic with an in-house proprietary process. This process modifies the surfaces of the individual fibers which make up the GDL. The resulting hydrophilic chemistry remains stable for more than 10,000 h under fuel cell operating conditions. Further details on WT processes may be found in the patent literature.[18-20]

Scanning electron micrographs (SEMs) of both as-received materials are presented in Fig. 1. Both GDLs are constructed of carbon fibers and resin. However, AR-Toray is composed almost entirely of fibers 7 μm in diameter, while AR-MRC has both 7 and 4 μm diameter fibers. Backscattered SEM images, not shown here, highlight the role of phenolic resin at the junction of fibers in AR-Toray.

* Electrochemical Society Student Member.
** Electrochemical Society Active Member.
z E-mail: kevin.gallagher@chbe.gatech.edu

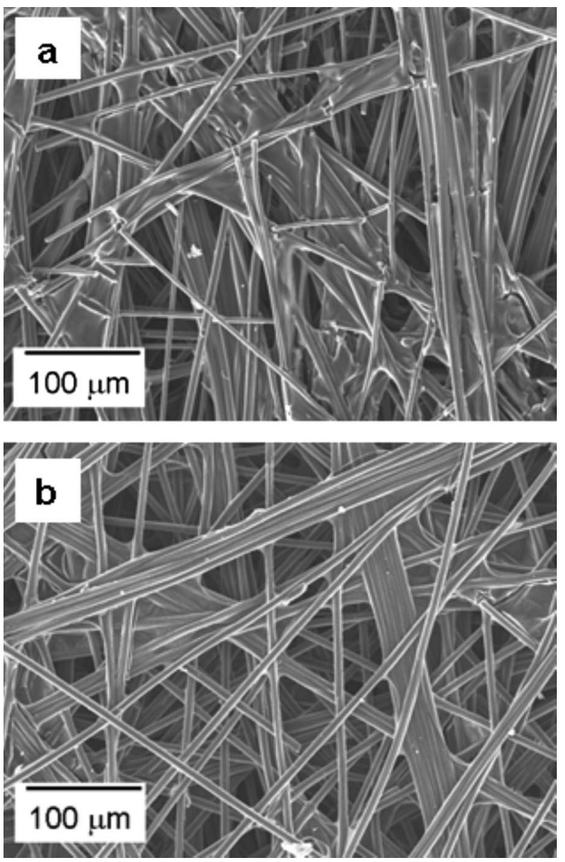

Figure 1. SEM of GDLs: (a) AR-MRC and (b) AR-Toray.

Regions of resin can be observed with diameters as large as 500 μm in AR-Toray samples but are not evident in the backscattered images of AR-MRC.

MIP.— Mercury intrusion porosimetry (MIP) was performed on both samples by Micromeritics Instrument Corporation. A mercury-GDL contact angle of 130° was used for the analysis. Volumes attributed to pore diameters greater than half of the GDL sample width were considered an experimental artifact and were discarded. The MIP technique has been used extensively in the soil science community where the pores are often formed by spherically shaped particles. In this environment, MIP with the Y-LE determines the characteristic cylindrical pore size. Narrow pore throats shield larger openings, incorrectly attributing pore volume to smaller characteristic radii.[21] From Fig. 1, the geometry of the GDLs is clearly different than the pore throat and openings observed in soil science. At the porosities of the GDLs used, ~75%, shielding is most likely less of a concern. Although uncertainties exist as a result of differences in pore openings, estimation of contact angles, large pressures, and mixed wettability, MIP provides a valuable source of comparison for the CPSRs reported within.[15]

Saturation measurements.— In order to measure the CPSR, we employed the use of water transport plate (WTP) technology. A WTP is a finely porous hydrophilic carbon plate. The WTP technology, as practiced by UTC Power, is discussed by Yi et al. and evaluated with a numerical model by Weber and Darling.[22,23] For our experimental purposes, we placed a 3.8 × 5 cm GDL between two of the WTPs. The experimental apparatus is illustrated in Fig. 2. In the bottom WTP, water flows through the internal coolant channels below atmospheric pressure; hence, the WTP is maintained at positive capillary pressures. This water may flow to and from the GDL

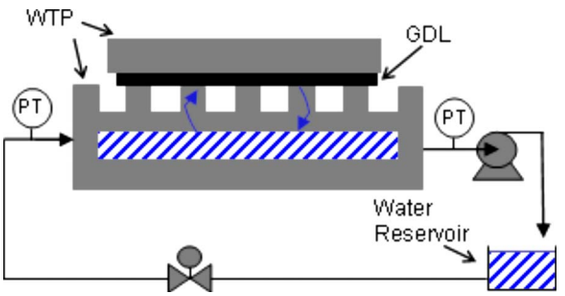

Figure 2. (Color online) Experimental apparatus for measuring CPSRs. PT: pressure transducer.

through the porous WTP if the capillary pressure in the GDL is different than capillary pressure in the WTP and should equalize the capillary pressures at long times. Because the WTP has a small pore radius and contact angle, the WTP remains completely saturated, to a good approximation, over a large range of capillary pressures. This plate also has channels adjacent to the GDL that are open to ambient air, ensuring a constant gas pressure of 101.3 kPa. A separate WTP without channels was placed on top of the GDL to prevent evaporation and provide a small force to ensure contact between the GDL and the base WTP. Although the role of compression on CPSRs has been shown, we neglected the effect during this discussion.[10] The top WTP resulted in a pressure of 70 Pa on the GDL. The top WTP was first allowed to equilibrate with the capillary pressure of the base WTP before the GDL was placed in between. The liquid pressure is controlled by a valve and pump on the coolant flow line which circulates between the WTP and a small reservoir which is open to the atmosphere. Saturation levels in GDLs were measured at capillary pressures from 0 to 25 kPa. GDL samples were from the same respective supplier manufacturing run. Run-to-run variability is not expected to change the conclusions found in this work.

The time constant for equilibration may be estimated using a time-dependent material balance equation. The details of the derivation are provided in the Appendix. The characteristic time, t^*, is shown in Eq. 3, where all fluid properties are that of water. Here, ε_o is the bulk porosity of the GDL and μ is the viscosity of water. L is half the width of a gas channel in the WTP, the largest characteristic dimension. The product of the saturated permeability, k, and the relative permeability K_w, is equivalent to the permeability at the saturation of interest. The slope of the CPSR, $\partial S_w/\partial P_w$, was first approximated and later compared with the measured results

$$t^* = \frac{\varepsilon_o \mu L^2}{K_w k} \frac{\partial S_w}{\partial P_w} \qquad [3]$$

The largest characteristic time over the CPSR is on the order of seconds. To ensure equilibrium, we waited at least 10 min before removing the sample. Afterward, the samples were removed from the WTP and sealed in a polyethylene bag to avoid evaporation. The bag was then weighed on an analytical balance. This procedure was repeated at the next capillary pressure. The minimum change in capillary pressure between data points was 1.5 kPa to prevent significant effects as a result of internal GDL water movement after removal from the WTP. Multiple boundary drainage and imbibition curves were measured to present a continuous and complete set of data. At conditions near fully saturated, a small amount of water was left in the bag during the weighing and transfer processes. This mass was never found to be greater than 6 mg, or 0.5% of the total water mass in the GDL.

Each point at a presented capillary pressure was the average of three GDLs at three slightly different pressures with a total separation of 0.6 kPa. The liquid pressure dropped along the WTP due to the pressure drop in the interior flow channels. The inlet and exit pressures were monitored. The pressure for each GDL sample was

found by assuming laminar flow, which was reasonable at the low flow rates used, 50–80 cm^3/min. The largest difference in measured saturation between the samples occurred at the steepest point in the CPSR and after a vacuum fill.

To determine the saturation, we first determined the pore volume. This was accomplished by utilizing a liquid with a low surface tension, isopropyl alcohol (IPA) or octane, which was wicked into the pores of the GDL. Due to the low surface tension, it was reasonable to assume complete saturation. By measuring the increase in weight or mass of fluid in the pores, m_f, and using the known fluid density, ρ_f, the pore volume was simply

$$V_p = \frac{m_f}{\rho_f} \quad [4]$$

The skeletal density of the GDL, ρ_{sk}, which is related to the porosity,[2] was determined from Eq. 4, the dry sample mass, m_s, and the geometric sample volume, V_s

$$\rho_{sk} = \frac{m_s}{V_s - V_p} \quad [5]$$

The skeletal densities of Toray and MRC were found to be 1.91 and 1.67 g/cm^3, respectively. These values correspond to a bulk porosity of 73% for Toray and 81% for MRC.

Vacuum fill.— To achieve a saturated GDL, $S_w > 0.9$, the pores of the GDL were vacuum filled with water. The GDL was submerged in deionized water and weighted to prevent the sample from floating. Then the vessel was sealed in a chamber which was repeatedly brought under vacuum. The expansion of gas in the low-pressure environment caused bubbles to exit the GDL and rise out of the liquid bath. When the system pressure was returned to atmospheric, water filled the pores that once held the gas that had since escaped. Because the GDL was submerged, there was no pathway for gas to re-enter the pores. After multiple repetitions, a high saturation level was achieved which compared closely with that achieved with IPA. The vibrations from the connected vacuum pump most likely assisted with the removal of gases while the sample was submerged.

Results

The drainage and imbibition curve for AR-Toray are presented in Fig. 3. The drainage curve from a vacuum-filled sample undergoes the steepest drop in saturation near a capillary pressure of 5 kPa. For capillary pressures greater than 9 kPa only a slow decline of saturation occurs. This behavior is a result of the majority of pore volume in Toray being distributed near a single pore radius. The remaining saturation at capillary pressures greater than 20 kPa corresponds to small hydrophilic pores and trapped water that will be removed upon further cycling. The residuals of the drainage curve fit, measured minus fitted, are shown in the inset of Fig. 3. These values are taken from the individually measured samples to determine the goodness of fit. The scatter is reasonably even, with some deviation at low capillary pressures. All of the residuals, ΔS_w, are $\leqslant 0.08$ units of saturation. The majority of scatter is attributed to slightly different states of initial saturation. As we discuss throughout this work, the wetting history of the sample determines the drainage or imbibition path it will follow.

The imbibition from a dry AR-Toray sample is delayed until capillary pressures approach zero. The imbibition for a vacuumed-filled sample that was drained to 20 kPa exhibits a similar shape to the dry sample. An increase in saturation only occurs at capillary pressures near zero. The saturation at zero capillary pressure for the initially dry sample is half the value for the sample that was vacuum filled and subsequently drained. This hysteresis as well as the difference in imbibition and drainage curves are commonly found in porous media. The cause of hysteresis has been attributed to a number of mechanisms. On rough or heterogeneous media like the GDLs used here, the contact angle is larger for an advancing fluid when compared to a receding fluid.[5,24,25] In situations such as this

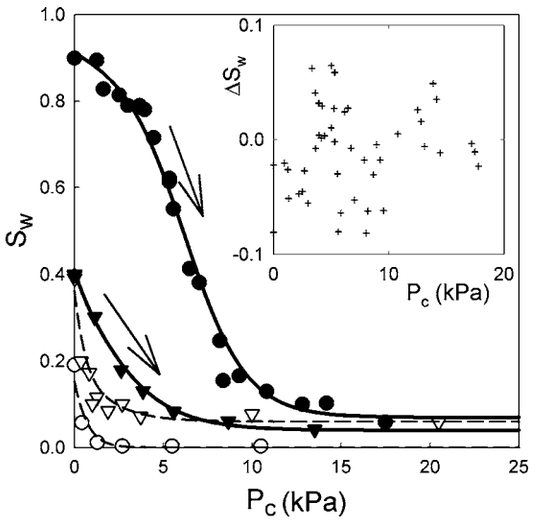

Figure 3. Drainage and imbibition curves for AR-Toray. Solid circles are experimentally measured drainage saturations initiated after a vacuum fill. Open circles are measured imbibition saturations starting from a dry sample. Open triangles are imbibitions starting from a sample that was initially vacuum filled and drained to 20 kPa. The solid triangle curve is the drainage from the open triangle imbibition. Inset figure presents the residuals of individually measured S_w from that predicted by the fit for the drainage after a vacuum fill.

one, where the receding contact angle appears to be less than 90° and the advancing angle is greater than 90°, the decision to arbitrarily define one phase as the wetting phase is justified. Geometrical factors such as pore shape also result in preferential filling or drainage, resulting in a different capillary pressure for the same saturation.[5]

This behavior of water in the GDL pores is further investigated by draining the sample from various levels of saturation. After filling the sample to 0 kPa, a draining scanning curve is traced by raising the capillary pressure. This draining curve crosses over the imbibition curve the sample had previously traced, resulting in a lower saturation at the same capillary pressure. AR-Toray appears to have only a small irreducible wetting saturation, $S_w^0 = 0.01$.

The role of hysteresis may be studied more completely in this apparatus with a sample that has a greater hydrophilic nature. The CPSR for a WT-Toray sample is presented in Fig. 4. The drainage curve is almost identical to that of the AR-Toray. However, the residuals for the WT-Toray displayed in the inset of Fig. 4 are less on average and more evenly distributed when compared to AR-Toray. The WT process may provide for a consistent and more uniform surface chemistry than what is found in as-received samples. All residuals for the WT-Toray are $\leqslant 0.05$ units of saturation. The lower run-to-run variability of the WT-Toray will also enable a more precise analysis of hysteresis in GDLs. During imbibition from a dry sample, the saturation reaches 0.85 at 0 kPa, which is four times higher than the AR-Toray. The WT process significantly decreases the contact angle between water and the GDL. This decrease in contact angle allows a greater fraction of the pores to be filled at a higher capillary pressure. The wetting treatment also significantly reduces the differences between the imbibition and drainage curves. Because the drainage curve is not shifted from the AR-Toray sample, we may conclude the advancing contact angle undergoes a greater change than the receding angle. The nature of the advancing contact angle changes from being larger than 90° and hydrophobic to less than 90° and hydrophilic. However, the existence of some hysteresis is still evident.

Several drainage curves from different saturations are displayed in Fig. 4. As the saturation decreases, the drainage curve asymptotically approaches the main drainage curve or boundary curve. The

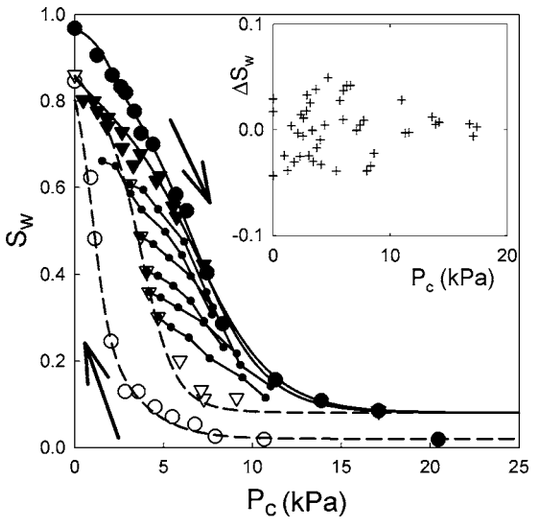

Figure 4. Drainage and imbibition curves for WT-Toray. Solid circles are experimentally measured drainage saturations. Open circles are measured saturations for imbibition from a dry GDL. Open triangles are measured saturations for imbibition from a vacuum-filled and subsequently drained GDL. Inset figure presents the residuals of individually measured S_w from that predicted by the fit for the drainage after a vacuum fill.

drainage curves starting from saturations other than fully wetted are commonly referred to as drying scanning curves. The imbibition from a saturation other than the irreducible wetting saturation are termed wetting scanning curves.[5] Clearly, the wetting and dewetting history of the sample is of great importance.

The CPSR for AR-MRC is not significantly dissimilar from AR-Toray over the range of capillary pressures measured (Fig. 5). The shape of the drainage shows a different slope, suggesting a moderately different pore distribution. However, the WT-MRC drainage curve is significantly different when compared to the other drainage curves. At high capillary pressures, the saturation level is twice the value of the AR-MRC. By WT the GDL, we have observed behavior about the pore structure of the hydrophobic components which would be inaccessible without large negative capillary pressures.

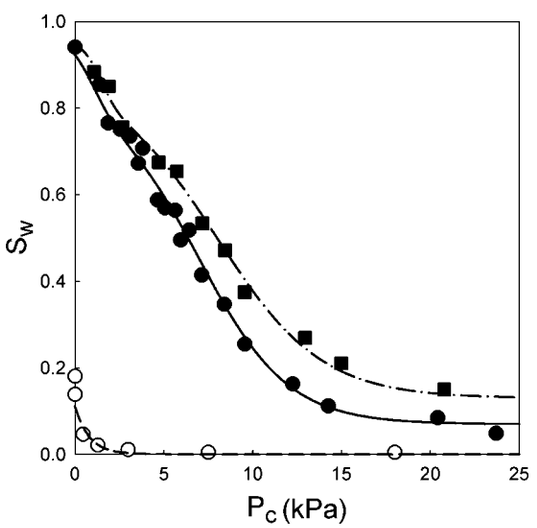

Figure 5. Drainage and imbibition curves for MRC. AR-MRC: Solid circles are experimentally measured drainage saturations, and open circles are measured imbibition saturations. WT-MRC drainage curve is solid squares.

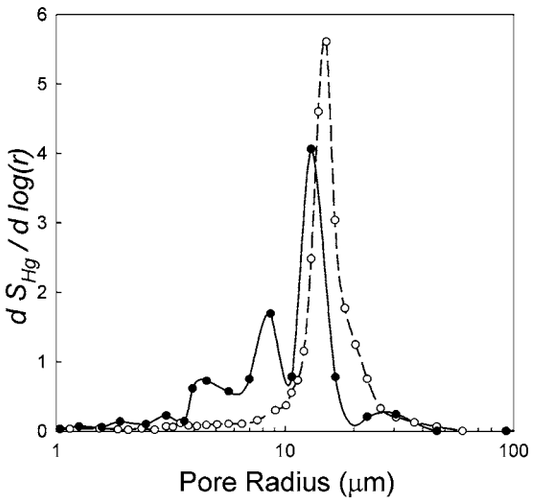

Figure 6. Characteristic pore radius as determined by MIP.

These results suggest that the moderate saturation at high capillary pressures is a result of small pores which are normally of a hydrophobic nature.

Discussion

Distribution of pore sizes and surface energy.— We can make some determinations about the pore distribution as a function of capillary pressure by analyzing the CPSR for the AR as compared to the WT samples. The pore radii may be approximately determined by using a liquid with a known contact angle such as mercury or wetting solvents such as octane. This approach requires the use of the Y-LE and the assumption that the pores are adequately modeled by capillaries. From Fig. 1, the pores do not appear to be cylindrical; therefore, we acknowledge an unquantifiable error is introduced into the discussion. The pore distribution as determined by MIP is displayed in Fig. 6. Toray appears to have symmetric distribution of pores with an average characteristic radius of 15 μm, which is within the range of reported values of 9–20 μm.[2,15] MRC appears to have a broader micrometer pore distribution of similar radius to Toray. However, MRC also has a distribution of smaller pores. Because the WT-MRC sample had a greater saturation at higher capillary pressures than the AR-MRC sample, we suggest the smaller pore radii displayed in MIP are of hydrophobic nature in the AR-MRC.

In the discussion of porous media, it is common to assign a distribution of pores as hydrophobic, $\theta > 90$, or as hydrophilic, $\theta < 90$. This simplification allows for a physical model with the following conclusions. Small hydrophilic pores fill at high positive capillary pressures with larger hydrophilic pores also filling at low positive capillary pressures. For hydrophobic contact angles, large pores fill at small negative capillary pressures followed by small pores being filled at large negative capillary pressures. Thus, at high negative capillary pressures, all pores will be filled. In this model, a capillary pressure of zero equates to all of the hydrophilic pores being filled and all of the hydrophobic pores being drained. However, we have shown the majority of the pore volume in the AR-GDLs behaves as a hydrophobic pore during imbibition and as a hydrophilic pore during drainage. Thus, broad classifications of pores and their surface energies should only be made under well-defined circumstances.

Empirical CPSR fit.— To assist with the use of the experimentally measured CPSRs, we have fit the data with the use of a hyperbolic tangent function. No physical meaning is strictly ascribed to

Table I. Parameters for curve fits to CPSRs.[a]

GDL	Curve	Initial condition	A_-	B_-	A_+	B_+	S_+^0	S_-^0	f_+
AR-Toray	D	VF	0.3	−1.5	0.29	−6.2	0.07	0.0	0.9
	I	VF, D to 20 kPa	0.31	0.5	1.1	0.38	0.06	0.05	0.7
	I	Dry	0.6	−3.0	0.8	0.8	0.0	0.05	0.7
WT-Toray	D	VF	1.0	−2.0	0.25	−6.5	0.08	0.0	0.9
	D	I to 0 kPa	0.4	0.05	0.23	−6.8	0.08	0.05	0.85
	I	Dry	1.0	−1.0	0.3	−2.0	0.02	0.05	0.35
	I	D 20 kPa	0.3	−2.0	0.6	−3.9	0.08	0.05	0.57
AR-MRC	D	VF	0.7	−1.0	0.2	−7.0	0.07	0.0	0.82
	I	Dry	0.2	9.0	0.7	1.3	0.0	0.05	0.8
WT-MRC	D	VF	1.0	−1.5	0.17	−8.0	0.13	0.0	0.85

[a] AR: as-received; WT: wet-treated; D: drainage; I: imbibition; and VF: vacuum fill.

the variables, except for the capillary pressure, P_c, and wetting saturation, S_w. The following equations are used as an empirical representation of the CSPRs we have measured

$$S_- = \frac{1}{2}[1 + \tanh(-A_-[P_c + B_-])] \quad [6]$$

$$S_+ = \frac{1}{2}[1 + \tanh(-A_+[P_c + B_+])] \quad [7]$$

$$S_w = S_+^0 + (1 - S_+^0 - S_-^0)[f_+S_+ + (1 - f_+)S_-] \quad [8]$$

All saturations at negative capillary pressures are our predictions based upon the measured CPSRs from the wet-treated samples and MIP. Nonetheless, the Toray predictions compare favorably with those reported by Fairweather et al., who used a technique that enabled measurements of saturation at negative capillary pressures.[16] The researchers found that the imbibition and drainage curves for AR-Toray are of nearly identical shape, but offset from each other. Table I summarizes the parameter values for MRC and Toray. A comparison for the full drainage and imbibition curves for AR-Toray and AR-MRC is shown in Fig. 7.

Contact angle hysteresis.— Using the Y-LE and the measured CPSR, the contact angle for imbibition and drainage may be estimated for AR-Toray. The results are shown in Table II using a pore radius of 15 μm estimated from MIP porosimetry and a radius of 12 μm reported from capillary flow porometry,[3] the capillary pressure at the steepest point in the CPSR, and the surface tension of water, 0.072 N/m. The use of pore radii determined from two separate techniques demonstrates the order of uncertainty. The values for a graphite fiber and poly(tetrafluoroethylene) (PTFE) from Penn and Miller and the values for two polyacrylonitrile (PAN) based carbon fibers from Bismarck et al. as measured with the Wilhelmy balance principle are also displayed.[26,27] Toray and the graphite fiber have similar contact angles and hysteresis between advancing and receding. Some uncertainty exists in the use of the Y-LE and in the exact contact angle measurements for graphite fiber made by Penn and Miller.[26] Furthermore, differences in the surface chemistry of the fibers has a direct impact on the surface energy and resulting contact angles.[27] However, the majority of hysteresis observed in the CPSR may be reasonably attributed to this difference in advancing and receding contact angle.

Using the sessile drop method on the surface of Toray, researchers have reported an effective contact angle of 112° for water on Toray.[15] This effective contact angle is a value corrected for the roughness and porosity of the GDL.[28] The applicability of an external contact angle measurement is unclear when compared to the values in Table II. The contact angle which controls the imbibition and draining process is more appropriately measured between two fibers. In this scenario, the angle of the fiber intersection and the advancing and receding nature of the contact angle are important.[29] However, this measurement is challenging at the length scales of GDL pores. The values obtained from a single fiber appear to be more significant than that of an external contact angle.

In order to maintain sufficient porosity for gaseous diffusion, GDLs are often wet-proofed with materials such as PTFE. This treatment increases the contact angle as a result of the low surface energy of the PTFE. The process of wet-proofing GDLs typically results in an anisotropic coating producing a bimodal pore network.[9,15] One pore network resembles that of the AR sample due to a minimal or nonexistent PTFE content. The other pore network may have a changed porosity and certainly lower surface energy from the PTFE coating.[9] The increase in advancing and receding contact angle should shift the CPSR to more negative capillary pressures. A close inspection of the wet-proofed results of Fairweather et

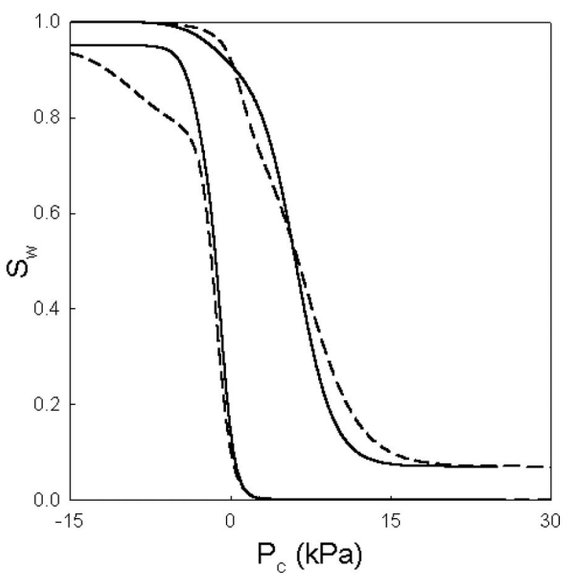

Figure 7. Comparison of CPSRs for AR-Toray (solid line) and AR-MRC (dashed line).

Table II. Advancing (θ_a) and receding (θ_r) contact angles.

Material	θ_a (°)	θ_r (°)	$\theta_a - \theta_r$ (°)	Source
Toray (15 μm)	98	51	47	This work
Toray (12 μm)	96	59	37	This work
PAN fiber	80	48	32	Ref. 27
PAN fiber	83	56	27	Ref. 27
Graphite fiber	94	45	49	Ref. 26
PTFE	112	92	21	Ref. 26

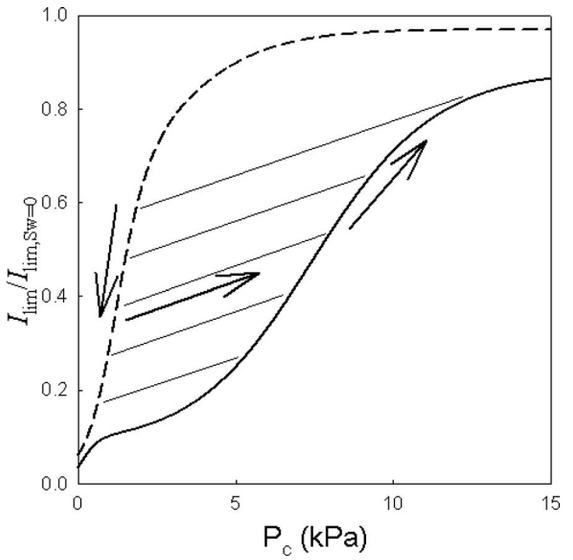

Figure 8. Change in WT-Toray dimensionless limiting current based upon history of wetting. Imbibition is the dotted line and drainage is the solid line. Arrows demonstrate the filling and subsequent draining path of hypothetical PEMFC operation.

al. reveals an offset in the CPSR where saturation moves from one pore network to the other during imbibition.[16] The hysteresis demonstrated in this paper is directly applicable to wet-proofed GDLs. Even on a smooth and well-defined PTFE surface, contact angle hysteresis is still observed (see Table II).[26] The averaging of two CPSRs, one for the as-received network and another shifted slightly to more negative capillary pressures, will prove an adequate approximation of the dual pore network of wet-proofed GDLs.

Effect on limiting current.— The effect of saturation and wetting history on the limiting current in a PEMFC may be considered. If we consider an isothermal situation where the limiting current is controlled by diffusion of oxygen through the GDL, the ratio of the flux of oxygen in the GDL with a specified saturation to flux of oxygen in a dry GDL is equivalent to the ratio of limiting currents under the same conditions. Assuming Fickian diffusion of dilute oxygen or the diffusion of oxygen through a stagnant mixture, Eq. 9 describes the molar flux

$$N_{O_2} = -\frac{\varepsilon_o(1 - S_w)D_{O_2}P}{\tau RT}\nabla y_{O_2} \quad [9]$$

P and T are the system pressure and temperature. R is the ideal gas constant and D_{O_2} is the diffusion coefficient of oxygen. The porosity, ε, is equivalent to the product of the bulk porosity, ε_o, and the nonwetting saturation, $(1 - S_w)$. The tortuosity, τ, is that considered by Bruggeman to be equal to $\varepsilon^{-0.5}$. The use of Fickian diffusion and the Bruggeman correlation is an oversimplification of actual transport through the GDL. The goal of this empirical analysis is to present a basic demonstration of the effect of hysteresis on the limiting current as might be observed during the measurement of a polarization curve. The ratio of fluxes simplifies to

$$\frac{I_{lim}^{S=S_w}}{I_{lim}^{S=0}} = \frac{N_{O_2}^{S=S_w}}{N_{O_2}^{S=0}} = (1 - S_w)^{1.5} \quad [10]$$

The ratio of limiting currents is plotted in Fig. 8 for both the drainage and imbibition curves for WT-Toray. A ratio of limiting currents near unity represents a low saturation level, while a ratio near zero is indicative of a flooded GDL. Depending on whether the GDL is being filled or drained, the dependence of the limiting current with saturation and thus time will change.

Water management.— An alternative approach to water management in PEMFCs is to actively control the capillary pressure at the boundary of the WTP and the GDL. By holding the WTP at sufficiently high capillary pressures, the GDL saturation is maintained near the irreducible saturation. Furthermore, WTPs create a 100% relative humidity environment while also controlling liquid water transport.[23]

Conclusions

Measured hysteresis in CPSRs for PEMFC GDLs produced by Toray and Mitsubishi Rayon is presented. The hysteresis is primarily a result of the difference in the advancing and receding contact angle of water on the carbon fibers which compose the GDL. This hysteresis is shown to have a direct impact on the limiting current of PEMFCs.

If the wetting history of the sample is accounted for, modeling the saturation level becomes substantially more difficult. To avoid an almost infinite set of boundary conditions, a closed form relation that predicts both static and dynamic capillary hysteresis, such as that presented by Beliaev and Hassanizadeh, may be necessary.[30] If PEMFC models continue to neglect the effect of wetting history, the order of error involved needs to be quantified. Future work involving CPSRs should focus on understanding phenomena which results in effects on the same order of the hysteresis presented within this work or on the presence of hysteresis itself.

Acknowledgments

SEMs of Toray and MRC were provided by Bob Brown and Dave Condit at the United Technologies Research Center, East Hartford, Connecticut 06108, USA.

UTC Power assisted in meeting the publication costs of this article.

Appendix

The time constant for equilibration may be estimated using a time-dependent material balance equation

$$\varepsilon_o\frac{\partial \rho S_w}{\partial t} = -\nabla \cdot \rho v_0 \quad [A\text{-}1]$$

The wetting fluid may be considered incompressible and thus, density of water, ρ, is considered constant. Darcy's law provides the volumetric flux of the wetting fluid

$$v_0 = -K_w\frac{k}{\mu_w}\nabla P_w \quad [A\text{-}2]$$

The absolute permeability for Toray is 9×10^{-12} m^2.[31] The relative permeability of the wetting phase is expressed as

$$K_w = S_w^n \quad [A\text{-}3]$$

The value of n has been reported as a range of values, typically 3–9. Here, we conservatively chose $n = 5$. Substituting Eq. A-1 into Eq. A-2 and assuming an isotropic permeability results in

$$\varepsilon_o\frac{\partial S_w}{\partial t} = K_w\frac{k}{\mu_w}\nabla^2 P_w \quad [A\text{-}4]$$

To reach the characteristic time constant, $t^* = t/\Theta$, we assume transport occurs only in the x dimension, and scaling with the largest characteristic dimension, L, we have $X = x/L$. Here Θ is the dimensionless time and X is the dimensionless length. Furthermore, using the chain rule

$$\frac{\partial S_w}{\partial t} = \frac{\partial S_w}{\partial P_w}\frac{\partial P_w}{\partial t} \quad [A\text{-}5]$$

we arrive at the characteristic time

$$t^* = \frac{\varepsilon_o\mu_w L^2}{K_w k_w}\frac{\partial S_w}{\partial P_w} \quad [A\text{-}6]$$

List of Symbols

A	parameter for CPSR fit, kPa^{-1}
B	parameter for CPSR fit, kPa
D_i	diffusion coefficient of species I, cm^2/s
f_i	fraction of S_w attributed to S_i
I_{lim}	limiting current, A/cm^2
k	absolute permeability, cm^2

K	relative permeability
L	characteristic length, cm
m	mass, g
n	constant
N_i	flux of species I, mol/cm^2 s
P	pressure, kPa
r	pore or capillary radius, cm
R	universal gas constant, 8.3144 J/mol K
S	saturation
t	time, s
T	absolute temperature, K
v_0	volumetric flux, cm^3/cm^2 s
V	volume, cm^3
X	dimensionless length
y_i	mole fraction of species i

Greek

γ	surface tension of wetting fluid, dynes/cm
Δ	residual, measured value–fitted value
ε	porosity
θ	contact angle, degrees
Θ	dimensionless time
μ	viscosity, cp
ρ	density, g/cm^3
τ	tortuosity

Subscripts

a	advancing
c	capillary
f	fluid
nw	nonwetting
o	bulk
p	pore
s	sample
sk	skeleton
w	wetting

Superscripts

0	residual
*	characteristic

References

1. T. F. Fuller and J. Newman, *J. Electrochem. Soc.*, **140**, 1218 (1993).
2. M. Mathias, J. Roth, J. Fleming, and W. Lehnert, *Handbook of Fuel Cells–Fundamentals, Technology and Applications*, W. Vielstich, H. A. Gasteiger, and A. Lamm, Editors, Vol. 3, Chap. 46, John Wiley & Sons, Ltd., New York (2003).
3. A. Z. Weber and J. Newman, *Chem. Rev. (Washington, D.C.)*, **104**, 4679 (2004).
4. C. Y. Wang, *Chem. Rev. (Washington, D.C.)*, **104**, 4727 (2004).
5. J. Bear, *Dynamics of Fluids in Porous Media*, Dover Publications, Inc., New York (1988).
6. H. Li, Y. Tang, Z. Wang, Z. Shi, S. Wu, D. Song, J. Zhang, K. Fatih, J. Zhang, H. Wang, et al., *J. Power Sources*, **178**, 103 (2008).
7. A. Z. Weber, R. M. Darling, and J. Newman, *J. Electrochem. Soc.*, **151**, A1715 (2004).
8. Y. M. Volfkovich, V. S. Bagotzky, V. E. Sosenkin, and I. A. Blinov, *Colloids Surf., A*, **187–188**, 349 (2001).
9. E. C. Kumbar, K. V. Sharp, and M. M. Mench, *J. Electrochem. Soc.*, **154**, B1295 (2007).
10. E. C. Kumbar, K. V. Sharp, and M. M. Mench, *J. Electrochem. Soc.*, **154**, B1305 (2007).
11. E. C. Kumbar, K. V. Sharp, and M. M. Mench, *J. Electrochem. Soc.*, **154**, B1315 (2007).
12. J. H. Nam and M. Kaviany, *Int. J. Heat Mass Transfer*, **46**, 4595 (2003).
13. P. K. Sinha and C. Y. Wang, *Electrochim. Acta*, **52**, 7936 (2007).
14. J. T. Gostick, M. A. Ioannidis, M. W. Fowler, and M. D. Pritzker, *J. Power Sources*, **173**, 277 (2007).
15. J. T. Gostick, M. W. Fowler, M. A. Ioannidis, M. D. Pritzker, Y. M. Volfkovich, and A. Sakars, *J. Power Sources*, **156**, 375 (2006).
16. J. D. Fairweather, P. Cheung, J. St-Pierre, and D. T. Schwartz, *Electrochem. Commun.*, **9**, 2340 (2007).
17. T. V. Nguyen, G. Lin, H. Ohn, and X. Wang, *Electrochem. Solid-State Lett.*, **11**, B127 (2008).
18. J. A. S. Bett, D. J. Wheeler, and C. Bushnell, U.S. Pat. 5,840,414 (1998).
19. N. E. Cipollini, U.S. Pat. 6,258,476 (2001).
20. J. W. Frisk and W. M. Boand, U.S. Pat. 6,733,841 (2004).
21. M. A. Ioannidis and I. Chatzis, *Chem. Eng. Sci.*, **48**, 951 (1993).
22. J. S. Yi, D. Yang, and C. King, *AIChE J.*, **50**, 2594 (2004).
23. A. Z. Weber and R. M. Darling, *J. Power Sources*, **168**, 191 (2007).
24. C. W. Extrand and Y. Kumagai, *J. Colloid Interface Sci.*, **191**, 378 (1997).
25. R. J. Good, *J. Adhes. Sci. Technol.*, **6**, 1269 (1992).
26. L. S. Penn and B. Miller, *J. Colloid Interface Sci.*, **78**, 238 (1980).
27. A. Bismarck, R. Tahhan, J. Springer, A. Schulz, T. M. Klapotke, H. Zell, and W. Michaeli, *J. Fluorine Chem.*, **84**, 127 (1997).
28. A. B. D. Cassie and S. Baxter, *Trans. Faraday Soc.*, **40**, 546 (1944).
29. S. Ma, G. Mason, and N. R. Morrow, *Colloids Surf., A*, **117**, 273 (1996).
30. A. Y. Beliaev and S. M. Hassanizadeh, *Transp. Porous Media*, **43**, 487 (2001).
31. J. T. Gostick, M. W. Fowler, M. D. Pritzker, M. A. Ioannidis, and L. M. Behra, *J. Power Sources*, **162**, 228 (2006).